Very-high-energy afterglows from Gaussian structured jets in wind-driven media and prospects for the CTA detectability of events like GRB 221009A

Tanima Mondal,[1,*] Sabyasachi Chakraborty,[1] Lekshmi Resmi,[2] and Debanjan Bose[3]

[1]*Department of Physics, Indian Institute of Technology Kharagpur, Kharagpur, West Bengal 721302, India*

[2]*Department of Earth & Space Sciences, Indian Institute of Space Science & Technology, Trivandrum 695547, Kerala, India*

[3]*Department of Physics, Central University of Kashmir, Ganderbal, 191131, Jammu & Kashmir, India*

(Received 6 March 2026; accepted 21 July 2026; published 10 September 2026)

Recent detections of very-high-energy [(VHE) $\gtrsim$100 GeV] photons from afterglows like gamma-ray burst (GRB) 221009A demand models that treat jet angular structure, circumburst stratification, and inverse Compton radiation self-consistently. We present a numerical afterglow framework in which a Gaussian structured jet decelerates as an adiabatic forward shock in a wind-stratified medium ($\rho \propto r^{-2}$), and compute broadband synchrotron and synchrotron self-Compton (SSC) emission. Our approach aims to connect a wind-stratified environment with a Gaussian angular jet profile and to explore SSC emission to predict VHE afterglow detectability with the Cherenkov Telescope Array (CTA). We find that the TeV peak time and peak flux are primarily governed by jet geometry (ratio of θ_v/θ_c), together with wind-driven blast-wave deceleration and jet microphysics. In particular, variations in the jet kinetic energy (E_k), wind density parameter ($A_\star$), and the ratio of microphysical parameters (ϵ_e and ϵ_B) can change the TeV flux by orders of magnitude. Using the CTAO North differential sensitivity at 250 GeV, we simulate 4×10^4 wind-Gaussian afterglows and find that only $\sim$10% satisfy our detectability criterion, primarily for bursts with high E_k, moderate to high $A_\star$, high ϵ_e, and low ϵ_B, and near on-axis jet geometries ($\theta_v/\theta_c \lesssim 2$). Finally, fitting the multiband afterglow of GRB 221009A from radio to TeV, we obtain a mildly off-axis, SSC-dominated afterglow in a wind-driven medium that reproduces the observed broadband temporal evolution. The inferred parameters favor strong TeV SSC emission, implying that GRBs similar to GRB 221009A should be detectable by CTA.

DOI: 10.1103/yvg8-t64l

I. INTRODUCTION

Gamma-ray bursts (GRBs) are among the most luminous and energetic explosions in the Universe, releasing enormous amounts of energy across the electromagnetic spectrum [1,2]. Their broadband afterglow emission, from radio to x rays, is widely interpreted as synchrotron radiation from relativistic electrons accelerated in external forward shocks [1,3–8]. In recent years, detections of $\geq$ 100 GeV photons by ground-based Cherenkov telescopes have extended afterglow observations into the TeV regime [9–13]. These GeV-TeV detections strongly suggest the presence of an additional high-energy component consistent with synchrotron self-Compton (SSC) emission, where the same population of shock-accelerated electrons upscatters synchrotron photons to higher energies [14–24]. Interpreting very-high-energy (VHE) afterglow observations, therefore, requires consistent, refined theoretical models that self-consistently capture the shock dynamics, the microphysics of particle acceleration, radiative cooling, and angular jet structure.

The discovery of GRB 221009A has provided an unprecedented opportunity to explore such extreme regimes. Triggered by *Fermi*/GBM[1] on October 9 2022 at 13:16:59 UT (T_0) and located at a relatively low redshift ($z \sim 0.151$) [25,26], it stands among the brightest and most energetic long GRBs ever detected. The burst was extensively followed throughout the electromagnetic spectrum by *Swift* [27], *Fermi*-LAT [28], INTEGRAL/SPI-ACS, and Konus-Wind [29], with its localization refined through InterPlanetary Network triangulation [30]. Most notably, the Large High-Altitude Air Shower Observatory (LHAASO) detected photons exceeding 10 TeV [12,31], extending GRB emission observations into the multi-TeV domain. The broadband detection and long temporal baseline of GRB 221009A allow simultaneous constraints on the GRB jet structure, the circumburst density profile, and

*Contact author: mtanima14@gmail.com

[1]https://fermi.gsfc.nasa.gov/science/instruments/gbm.html

the mechanisms associated with high-energy radiation and particle acceleration.

Several studies have modeled multiband afterglows using both top-hat and structured jet outflows (power-law and two-component parametrizations) to interpret peak times, peak fluxes, and viewing-angle effects in broadband data [24,32–37]. In parallel, seminal studies established the standard afterglow dynamics and synchrotron and SSC emission for uniform outflows in both constant-density interstellar medium (ISM) and wind-stratified medium ($\rho \propto r^{-2}$) [38,39], which are commonly adopted as circumburst density profiles with windlike profiles being particularly motivated for massive-star progenitors. Along with top-hat, power-law, Gaussian, and multicomponent angular jet structures have been explored to understand viewing-angle effects and light-curve diversity [24,37,40] in GRB afterglow studies. Among the different jet structures, simple narrow top-hat jets can have difficulty reproducing TeV afterglows and the late-time broadband evolution simultaneously. In many models, their postpeak decay is too steep, especially if significant lateral expansion is assumed, leading to late-time fluxes that are too faint and restricting fits to the earliest epochs [32,33]. For GRB 221009A in particular, recent modeling has invoked structured outflows combined with high-energy radiation processes to account for the GeV-TeV afterglow, including shallow angular structures [37] and core-wing jet structure with possible density transitions [24]. These works illustrate that TeV-band light curves are sensitive to both jet angular structure and external density stratification, motivating a systematic study of how these components jointly regulate SSC peak evolution and detectability.

Although previous studies have modeled the multiwavelength afterglow of GRB 221009A using various structured jet configurations [24,34–36,41], a systematic investigation of the TeV SSC evolution and detectability for Gaussian jets in wind environments remains less explored. In contrast to earlier works, here we perform a systematic exploration of the structured jet parameter space to quantify how jet geometry, wind density, and microphysical parameters regulate the peak time, peak flux, and detectability of the TeV SSC afterglow. Motivated by these, we adopt a Gaussian structured jet evolving in an adiabatic forward shock propagating through a wind-driven medium. In a Gaussian angular profile, the kinetic energy per unit solid angle decreases smoothly away from the jet core, introducing a characteristic angular scale θ_c that determines the width of the jet core and regulates the transition from core-dominated on-axis to wing-dominated off-axis emission [42,43]. This smooth angular decline leads to a continuous dependence of the observed flux on the viewing angle θ_v, while the total jet energy remains finite and can be defined with a large outer cutoff angle without introducing a sharp discontinuity at the jet edge. As the blast wave decelerates in a wind medium ($\rho \propto r^{-2}$), the relativistic beaming cone widens, so progressively larger angular portions of the structured jet contribute to the observed flux. For a smooth Gaussian profile, this transition occurs gradually, which becomes particularly relevant for modeling off-axis and late-time behavior [24]. In the TeV regime, where SSC emission is sensitive to the jet kinetic energy per solid angle and the evolution of characteristic frequencies, the coupling between the Gaussian angular structure and wind-modified blast-wave dynamics plays a central role in shaping the peak time and high-energy peak flux.

Gaussian angular structures have been successfully employed to describe viewing angle–dependent afterglow evolution in structured jets [23,43]. In this framework, observers aligned near the jet core typically observe earlier and brighter peaks, while misaligned observers see delayed and dimmer emission, reflecting the combined effects of angular energy distribution and relativistic beaming. At TeV energies, where SSC emission dominates, the temporal evolution of the high-energy component is further influenced by the wind-driven deceleration law, the evolution of SSC characteristic frequencies, Klein-Nishina (KN) suppression, and correction due to extragalactic background light (EBL). Consequently, even moderate variations in jet core angle θ_c, viewing angle θ_v, wind density parameter, or microphysical parameters can significantly alter the peak time and flux level of the TeV afterglow. This sensitivity becomes especially evident when interpreting TeV observations with the Cherenkov Telescope Array (CTA), where slight changes in viewing angle, microphysics, and wind density parameter significantly impact detectability.

To address these aspects, we develop an afterglow model for a Gaussian structured jet evolving in a wind-driven medium and investigate the resulting VHE afterglow properties for both on- and off-axis observers. Our model integrates jet geometry (parametrized by the viewing to core angle ratio θ_v/θ_c), wind-modified blast-wave deceleration, and high-energy radiation processes, including synchrotron and SSC emission with KN suppression, internal $\gamma\gamma$ attenuation, and EBL absorption. Given the strong dependence of TeV light curves on jet geometry, wind density profile, kinetic energy, and microphysical parameters, we systematically explore the parameter space to quantify how these quantities regulate the afterglow peak time and peak flux. We then apply this framework to the broadband multifrequency observations of GRB 221009A, performing a joint fit to the radio, optical, x-ray, GeV, and TeV data using Markov chain Monte Carlo (MCMC) methods to constrain the jet and microphysical parameters within a wind-stratified environment.

The paper is organized as follows. In Sec. II, we present the off-axis Gaussian structured jet afterglow model in a wind-driven environment and outline its key features. Section III examines how the afterglow model parameters shape the TeV light curve. In Sec. IV we explore the detectability of TeV afterglows in a wind environment relative to the sensitivity of the CTA. To validate the framework, in Sec. V, we apply our Gaussian structured jet afterglow model to GRB 221009A, jointly fitting its x-ray, GeV, and TeV data in a wind medium. Finally, we summarize our results in Sec. VI.

II. AFTERGLOW EMISSION FROM STRUCTURED JET IN STELLAR WIND–DRIVEN MEDIUM

In this study, we develop a numerical framework to model the broadband afterglow emission from a Gaussian structured jet interacting with a stellar wind environment. We consider a relativistic jet propagating into a cold stellar wind–driven medium whose mass density profile follows a power-law form,

$$\rho(r) = Ar^{-2} = (5\times 10^{11} A_\star) r^{-2}\ \mathrm{g\,cm^{-1}}. \qquad (1)$$

Here, A is defined by the ratio of the mass-loss rate ($\dot{M}$) of the progenitor Wolf-Rayet star to the wind velocity (v_w). We adopt typical values $\dot{M} = 10^{-5} M_\odot\ \mathrm{yr}^{-1}$ and $v_w = 10^8\ \mathrm{cm\,s^{-1}}$ for a Wolf-Rayet star [38,44]. The dimensionless normalization parameter $A_\star$ characterizes the wind density profile of the stellar medium.

The corresponding radial number density of the wind is, therefore, given by

$$n(r) = \frac{A}{m_p} r^{-2} = \frac{5\times 10^{11} A_\star}{m_p} r^{-2} = n_k r^{-2}\ \mathrm{cm^{-3}}, \qquad (2)$$

where $n_k \sim (3\times 10^{35}) A_\star$ is the wind density normalization factor, m_p is the proton mass, and r denotes the radial distance from the central engine.

Within this framework, the relativistic Gaussian jet decelerates as it interacts with the stellar wind medium, driving a forward shock that accelerates electrons and amplifies magnetic fields. The shocked electrons radiate through synchrotron emission, while inverse Compton scattering of synchrotron photons produces SSC emission. Together, these processes generate broadband afterglow radiation extending from radio to TeV energies.

A. Jet structure and circumburst environment

In the stellar wind–driven medium, we model the evolution of a structured jet by retaining the intrinsic Gaussian angular structure $\{\mathcal{E}(\theta), \Gamma_0(\theta)\beta_0(\theta)\}$ identical to that adopted in Resmi *et al.* [43] and Mondal *et al.* [23]. Both the kinetic energy per unit solid angle and the initial Lorentz factor vary with polar angle and follow a Gaussian profile [42,43],

$$\mathcal{E}(\theta) = \mathcal{E}_c \exp\left(-\frac{\theta^2}{2\theta_c^2}\right), \quad \Gamma_0(\theta)\beta_0(\theta) = \Gamma_c\beta_c \exp\left(-\frac{\theta^2}{2\theta_c^2}\right). \qquad (3)$$

Here, $\mathcal{E}(\theta)$ represents the kinetic energy per unit solid angle, characterized by kinetic energy at jet core

$$\mathcal{E}_c = \frac{E_k}{\pi\theta_c^2(1 - e^{-\theta_j^2/\theta_c^2})},$$

where E_k is the total kinetic energy of the jet. The characteristic angle θ_c denotes the jet core width and determines the angular steepness of the jet structure. The initial velocity distribution of the jet is expressed through $\Gamma_0(\theta)\beta_0(\theta)$, which follows the same Gaussian angular profile.

In a wind-driven medium, only the radial evolution is modified according to the density profile $n(r) \propto r^{-2}$, while the angular structure remains unchanged. The inclination angle of a surface element at (θ_i, ϕ_k), as observed from a viewing angle θ_v, remains analogous to the ISM case [23] and is given by

$$\cos\alpha_{\mathrm{inc}}^{i,k} = \cos\theta_i \cos\theta_v + \sin\theta_i \sin\theta_v \cos\phi_k, \qquad (4)$$

where the polar angle spans from $0 < \theta_i < \pi/2$ and the azimuthal angle spans $0 < \phi_k < 2\pi$ with respect to the jet axis [23,43]. For each angular element (i, k), we consider the adiabatic evolution of the bulk motion of the ultra-relativistic ejecta as it propagates through the wind-driven medium as

$$\Gamma(\theta, r)\beta(\theta, r) = \Gamma_0(\theta)\beta_0(\theta)\left(\frac{r}{r_{\mathrm{dec}}}\right)^{-1/2}. \qquad (5)$$

In a stellar wind environment, the deceleration dynamics differ from the uniform ISM case because the swept-up mass per steradian increases linearly with radius [38]. The accumulated mass is $m(r) = \int 4\pi r^2 n(r) dr = 4\pi A r$, which leads to the deceleration radius

$$r_{\mathrm{dec}}^{\mathrm{wind}} = \frac{E_k}{4\pi n_k m_p c^2 \eta_c^2}. \qquad (6)$$

Here, $\eta_c = \Gamma_c\beta_c$ denotes the initial velocity at the jet core, m_p is mass of proton, and c is the speed of light. The deceleration radius r_{dec} of the jet is sensitive to the total kinetic energy E_k of the jet [39].

For a given radial profile, we estimate the observer-frame arrival time for each angular element (i, k) using the equal-arrival-time surface condition [45]. The observer time is written as

$$t_{\rm obs}(r,\alpha_{\rm inc}^{i,k}) = (1+z)\left[t_{\rm lab}(r) - \frac{r\cos\alpha_{\rm inc}^{i,k}}{c}\right], \qquad (7)$$

where $t_{\rm lab}(r)$ is the lab-frame time. Here, z is the redshift of the burst and the factor $(1+z)$ accounts for cosmological time dilation. For every angular element, we compute the observer-time relation $t_{\rm obs}(r,\alpha_{\rm inc}^{i,k})$ over a radial grid, as described in the revised Eq. (7). Therefore, at a fixed observer time, photons received from different angular elements generally originate from different radii because each element has a different inclination angle $\alpha_{\rm inc}^{i,k}$ with respect to the line of sight. In the numerical calculation, for a given range of r values, we interpolate the $t_{\rm obs}$-r array separately for each jet segment to obtain off-axis flux contribution from each jet segment at a given observer time [23,43]. The total observed flux is then obtained by summing the Doppler-boosted synchrotron and SSC contributions from all jet segments at that observer time. This procedure numerically accounts for the integration over the equal-arrival-time surface of the structured jet, considering all angular jet elements used in the off-axis structured jet afterglow calculation.

In the ultrarelativistic limit ($\Gamma \gg 1$), we adopt the approximations $\beta \simeq 1 - \frac{1}{2\Gamma^2}$ and $1-\beta\cos\alpha \simeq \frac{1}{2\Gamma^2} + \frac{\alpha^2}{2}$. For a stellar wind environment, the Lorentz factor evolves as $\Gamma(r) \propto r^{-1/2}$, which implies $r(t) \propto t^{1/2}$ and consequently $\Gamma(t) \propto t^{-1/4}$ [38].

From Eq. (6) we see that the dynamical deceleration radius in a stellar wind scales as $r_{\rm dec}^{\rm wind} \propto (\frac{\mathcal{E}_c}{\eta_c^2 A_\star})$, whereas in uniform ISM this deceleration radius scale as $r_{\rm dec}^{\rm ISM} \propto (\frac{\mathcal{E}_c}{\eta_c^2 n_0})^{1/3}$ [23]. This $r_{\rm dec}^{\rm wind}$ is typically a few orders of magnitude smaller than that in a uniform ISM for standard parameters because of the high initial density of the wind-driven medium. Although deceleration begins at a smaller radius (or earlier time) in a wind medium, the more gradual decline of the Lorentz factor Γ delays the emergence of off-axis emission, resulting in the off-axis peak occurring at a later time. The condition $\Gamma \sim 1/\theta_v$ is reached at a later observer time compared to the ISM.

B. Effect of a stellar wind medium on magnetic field strength, peak flux, and peak time

The afterglow peak flux across the broadband spectrum, from low-frequency radio to VHE gamma rays, is primarily governed by synchrotron and SSC emission. We consider an adiabatic forward shock expanding into a stellar wind–driven environment with a density profile $n(r)$ [Eq. (2)]. In the ultrarelativistic regime, the comoving postshock magnetic field strength for each angular jet element in the wind-driven medium is given by

$$B'(\theta,r) = (32\pi\epsilon_B\Gamma(\theta,r)^2 n(r) m_p c^2)^{1/2}. \qquad (8)$$

Electrons accelerated at the shock front are injected into a nonthermal power-law energy distribution, $N_e(\gamma) \propto \gamma^{-p}$ over $\gamma_m \le \gamma \le \gamma_{\rm max}$, where $p \gtrsim 2$. The minimum Lorentz factor of the injected electrons is $\gamma_m(\theta) = g(p)\epsilon_e(m_p/m_e)\Gamma(\theta)$, where $g(p) = (p-2)/(p-1)$ for $p > 2$. The cooling Lorentz factor is defined as $\gamma_c(\theta,r,t) = \frac{6\pi m_e c(1+z)}{(1+Y)\sigma_T B'(\theta,r)^2\Gamma(\theta)t_{\rm obs}}$, where Y is the Compton parameter representing the SSC-to-synchrotron luminosity ratio, σ_T is the Thomson cross section, and $t_{\rm obs}$ is the observer time. The maximum Lorentz factor, $\gamma_{\rm max}$, is obtained by balancing the acceleration timescale with the dominant cooling timescale, and it determines the high-energy cutoff frequency $\nu_{\rm max}$ of the synchrotron spectrum [46].

At low frequencies, synchrotron self-absorption becomes important. We, therefore, introduce the self-absorption Lorentz factor γ_a, corresponding to the electron Lorentz factor that emits predominantly at the self-absorption frequency ν_a. For given values of γ_m, γ_c, γ_a, and $\gamma_{\rm max}$ [46], the synchrotron spectrum is characterized by the standard break frequencies: the self-absorption frequency $\nu_a(\gamma_a)$, the injection frequency $\nu_m(\gamma_m)$, the cooling frequency $\nu_c(\gamma_c)$, and the maximum cutoff frequency $\nu_{\rm max}(\gamma_{\rm max})$ [22,23,46].

At relatively low frequencies, the Compton parameter Y is assumed to remain in the Thomson regime [22,47]. We calculate the low-frequency synchrotron flux by including the self-absorption prescription following Zhang [46], which improves the modeling of the radio-band light curves while leaving the high-frequency synchrotron and SSC formulation unchanged.

The synchrotron peak flux density for the wind density profile $n(r)$ can be estimated as

$$F_{\rm max}(R) = \frac{(1+z)}{d_L^2}\int_0^R n(r)4\pi r^2 P_{\nu,{\rm max}}(r)dr, \qquad (9)$$

where $P_{\nu,{\rm max}}(r)$ is the observed synchrotron peak spectral power per electron [6]. Accordingly, the peak flux density for each angular jet element (i,k) is obtained as

$$F_{\nu,{\rm max}}^{(i,k)}(R) = n_k \times R \times P_{\nu,{\rm max}}^{(i,k)}(R) \times \frac{\Omega_{i,k}}{\Omega_{e,i,k}} \times \frac{(1+z)}{d_L^2}. \qquad (10)$$

Here, R denotes the shock-front radius associated with the segment's deceleration radius $r_{\rm dec}$, and the ratio $\Omega_{i,k}/\Omega_{e,i,k}$ accounts for the fraction of the jet solid angle contributing to the observed emission from that segment following [42].

To relate the off-axis emission to the corresponding on-axis emission, we introduce the standard Doppler factor $\delta(r,\alpha_{\rm inc}^{i,k}) = \frac{1}{\Gamma(r)[1-\beta(r)\cos\alpha_{\rm inc}^{i,k}]}$ and define the Doppler ratio

$$a_{\rm dop}(r,\alpha^{i,k}_{\rm inc}) \equiv \frac{\delta(r,\alpha^{i,k}_{\rm inc})}{\delta(r,0)} = \frac{1-\beta(r)}{1-\beta(r)\cos\alpha^{i,k}_{\rm inc}}. \quad (11)$$

The observed off-axis synchrotron flux from each jet segment is then given by

$$F^{(i,k)}_{\rm syn,off}(t_{\rm obs},\alpha^{i,k}_{\rm inc},R) = a^3_{\rm dop}\cos\alpha^{i,k}_{\rm inc} \times F^{(i,k)}_{\nu/a_{\rm dop},{\rm on,max}}(R) f_{\nu_{\rm syn}}, \quad (12)$$

where $f_{\nu_{\rm syn}}$ represents the normalized on-axis synchrotron spectral profile for the slow- and fast-cooling regimes [6,46]. The observed frequency is correspondingly transformed as $\nu^{(i,k)}_{\rm off} = a_{\rm dop}(r,\alpha^{i,k}_{\rm inc})\nu_{\rm on}$.

C. Estimating SSC flux

Following Mondal *et al.* [23], the observed SSC flux from each angular jet segment (i,k) is estimated analogously to the synchrotron flux as

$$F^{(i,k)}_{\rm SSC}(R) = F^{(i,k)}_{\nu,\rm max}(R)(n_k R\sigma_T x_0) f_{\nu_{\rm SSC}}, \quad (13)$$

where $F^{(i,k)}_{\nu,\rm max}(R)$ represents maximum synchrotron peak flux along radius R for each of the jet segments, n_k is the wind density normalization constant, and σ_T is the Thomson scattering cross section. The factor $(n_k R\sigma_T)$ represents the effective optical depth for scattering in the wind-driven medium, while $x_0 = 0.5$ is adopted as the fractional scattering efficiency in the Thomson regime [16]. The on-axis SSC spectral profile $f_{\nu_{\rm SSC}}$ in both slow- and fast-cooling regimes is computed following Sari and Esin [16] and Zhang [46].

At very high photon energies, SSC scattering enters the KN regime, leading to suppression of the high-energy emission and modification of the spectral break structure [48]. We incorporate KN corrections within our structured jet wind model following the numerical prescription presented by Mondal *et al.* [23], which consistently accounts for the transition from the Thomson to the KN regime by introducing additional critical Lorentz factors and corresponding spectral breaks in the SSC component.

In a wind-driven medium, the radial evolution of the minimum and cooling electron Lorentz factors, γ_m and γ_c, differs from that in a uniform ISM due to the modified density profile $n(r) \propto r^{-2}$ [46]. Therefore, the strength of the KN correction and the corresponding Compton parameter $Y(\gamma)$ also evolve according to the wind-modified blast-wave dynamics. In this work, we incorporate the KN suppression of the SSC emission by following the prescription of Nakar *et al.* [48] and the detailed implementation presented in Mondal *et al.* [23], where the relevant critical Lorentz factors and the corresponding slow- and fast-cooling SSC spectral regimes are defined explicitly.

Finally, we include attenuation of VHE gamma-ray flux due to EBL absorption using the Domínguez EBL model [49]. This correction is essential for accurately modeling the observed TeV emission from GRB afterglows in a wind-driven environment.

III. IMPACT OF GAUSSIAN STRUCTURED JET AND AFTERGLOW PARAMETERS ON CHARACTERISTICS OF TEV LIGHT CURVE

In this section, we analyze the characteristics of TeV afterglows evolving in a stellar wind medium, as described in Sec. II. To assess the detectability of TeV afterglows by CTA, we choose an observed photon energy of 250 GeV as a representative TeV band and simulate the corresponding light curves. Figures 1–3 are, therefore, generated at this fixed observed photon energy. The wind afterglow model is governed by the jet structure parameters θ_c and θ_v, together with the physical afterglow parameters E_k, $A_\star$, ϵ_e, and ϵ_B. We systematically vary these quantities to examine their individual and combined influence on the TeV light-curve evolution, peak time, and peak flux.

A. Dependence on jet structure parameters

In a wind-driven medium, the density profile $n(r) \propto r^{-2}$ modifies the deceleration dynamics relative to a uniform ISM and consequently alters the evolution of relativistic beaming. To examine the role of jet geometry in shaping the TeV afterglow, we hold all physical parameters fixed and vary only the ratio θ_v/θ_c. The resulting light curves are shown in Fig. 1, revealing the influence of angular viewing

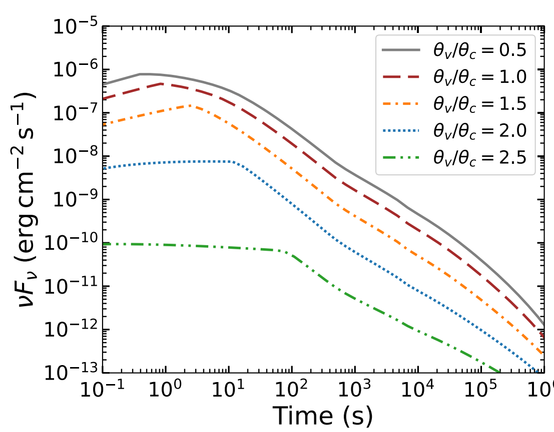

FIG. 1. Time evolution of the SSC afterglow flux at an observed photon energy of 250 GeV for a burst at redshift $z = 0.151$, shown for different jet geometries (θ_v/θ_c). The core angle is fixed at $\theta_c = 6°$, while the viewing angle is varied as $\theta_v = \{3°, 6°, 9°, 12°, 15°\}$, corresponding to typical on-axis to off-axis jet scenarios. The afterglow parameters are fixed to $E_k = 5.5\times10^{52}$ erg, $\eta_0 = 440$, $A_\star = 0.56$, $\epsilon_e = 0.1$, $\epsilon_B = 10^{-3}$, and $p = 2.5$. All SSC fluxes include the EBL correction.

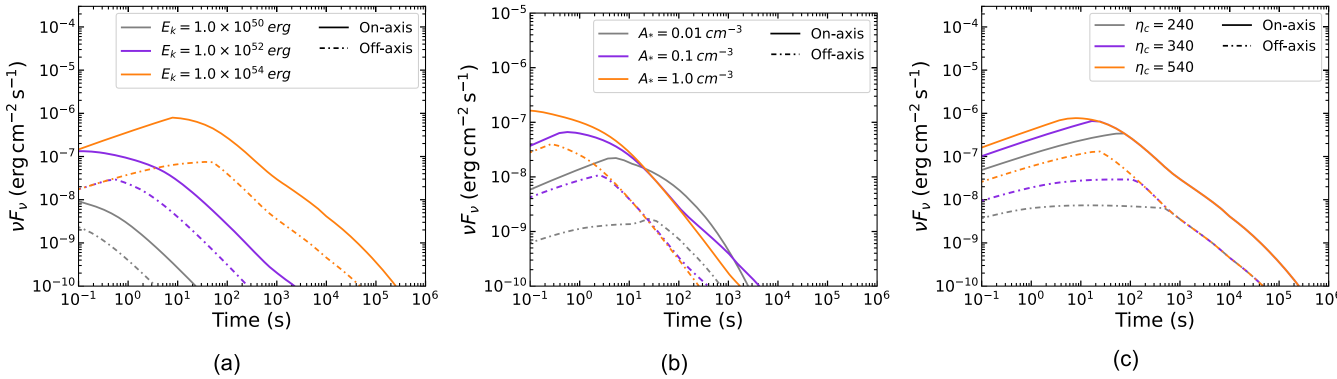

FIG. 2. SSC afterglow flux at an observed photon energy of 250 GeV for a burst at redshift $z = 0.151$ with varying parameters, as in (a) $E_k = \{10^{50}, 10^{52}, 10^{54}\}$ erg, (b) $A_\star = \{0.01, 0.1, 1.0\}$, and (c) $\eta_c = \{240, 340, 540\}$. Otherwise, parameters are fixed to $E_k = 10^{52}$ erg, $\eta_c = 440$, $A_\star = 0.56$, $\epsilon_e = 0.1$, $\epsilon_B = 10^{-3}$, and $p = 2.5$. For the on-axis case (solid curves) $\theta_v = 3°$ and for the off-axis case (dashed-dot curves) $\theta_v = 9°$, whereas θ_c is kept fixed at 6°. The light-curve plot depicts the SSC flux with EBL correction.

geometry on the timing and intensity of the TeV emission peak.

For a Gaussian structured jet, an observer at viewing angle θ_v sees different portions of the angular energy distribution as the blast wave decelerates and the relativistic beaming cone widens. The observed flux and peak time are governed by the Doppler factor and, therefore, depend sensitively on the ratio θ_v/θ_c. When the line of sight lies within the jet core ($\theta_v < \theta_c$), strong Doppler boosting produces earlier and brighter TeV peaks. In contrast, for off-axis geometry ($\theta_v > \theta_c$), Doppler deboosting delays the emergence of emission until $\Gamma \sim 1/\theta_v$, leading to dimmer light curves peaking at later epochs, as the beaming cone widens to confine the line of sight.

This angular dependence becomes particularly important in a wind environment because the deceleration radius

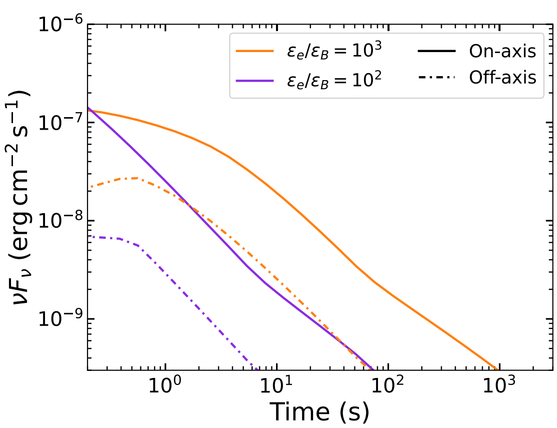

FIG. 3. SSC afterglow light curves at an observed photon energy of 250 GeV at redshift $z = 0.151$ for fixed $\epsilon_B = 10^{-3}$ and varying $\epsilon_e = \{0.1, 0.01\}$. Other afterglow parameters are fixed to $E_k = 10^{52}$ erg, $\eta_c = 440$, and $p = 2.5$. We show on-axis, solid curves ($\theta_v = 3°$), and off-axis, dashed-dot curves ($\theta_v = 9°$) cases, keeping fixed θ_c at 6°. Fluxes include attenuation by EBL correction.

scales differently than in a uniform ISM. As discussed in Sec. II, $r_{\rm dec}^{\rm wind} \propto \frac{\mathcal{E}_c}{\eta_c^2 A_\star}$, which directly shifts the characteristic timescale of the TeV peak. In the TeV regime, where the emission is SSC dominated, both Doppler boosting and the seed synchrotron photon field depend on the local kinetic energy per unit solid angle. Consequently, CTA detectability can vary by orders of magnitude depending on whether the observer is core-aligned or off-axis in a wind medium, making the ratio θ_v/θ_c a key predictor of observational outcome.

Figure 1 displays TeV light curves for $\theta_v/\theta_c = \{0.5, 1.0, 1.5, 2.0, 2.5\}$, with all other parameters fixed at $E_k = 5.5 \times 10^{52}$ erg, $A_\star = 0.56$, $\epsilon_e = 0.1$, $\epsilon_B = 10^{-3}$, $\eta_c = 440$, and $p = 2.45$, at redshift $z = 0.151$. Two robust trends emerge here. When the viewing angle lies within the jet core ($\theta_v < \theta_c$), strong Doppler boosting and the larger core kinetic energy per unit solid angle produce an early and bright TeV peak occurring near the onset of deceleration, with peak time scaling approximately as $t_{\rm pk} \sim t_{\rm dec}(\theta \approx 0) \propto \frac{\mathcal{E}_c}{A_\star \Gamma_c^4}$. As the viewing angle increases and the ratio θ_v/θ_c increases from 1.0 to 2.5 (dashed brown to dash-dot green), the viewing angle lies outside the jet core ($\theta_v > \theta_c$). Then, the light curve peaks shift to later times and the observed flux declines by several orders of magnitude due to enhanced Doppler deboosting. The emission becomes visible only when $\Gamma \sim 1/\theta_v$, thereby delaying the peak time. Simultaneously, both the kinetic energy per unit solid angle $\mathcal{E}(\theta_v)$ and the initial Lorentz factor $\Gamma_0(\theta_v)\beta_0(\theta_v)$ decrease exponentially with θ_v/θ_c, further suppressing the SSC emissivity. In this off-axis regime, the peak time shifts to progressively later times and the TeV emission becomes progressively fainter and more delayed as the observer becomes increasingly misaligned with respect to the jet core.

At late times ($t \gg t_{\rm pk}$), the blast wave becomes mildly relativistic, and the dependence on viewing angle weakens. The TeV light curves for different θ_v/θ_c values gradually converge toward similar decay slopes, determined primarily by adiabatic evolution in the wind density profile and the total jet energy. This convergence occurs more slowly than in a uniform ISM. In a wind medium, where the swept-up mass grows linearly with radius [$m(r) \propto r$], the Lorentz factor declines more gradually ($\Gamma \propto t^{-1/4}$), allowing angular differences in $\mathcal{E}(\theta)$ and $\Gamma_0(\theta)$ to persist over longer timescales before being smoothed out.

B. Dependence on afterglow parameters

Figures 2(a) and 2(b) illustrate how the TeV light-curve peak time and peak flux depend on variations in the total jet kinetic energy E_k and the wind density parameter $A_\star$, for both on-axis ($\theta_v < \theta_c$) and off-axis ($\theta_v > \theta_c$) geometry. In each panel, all parameters are held fixed except for the one being varied. As discussed in Sec. III A, for a wind density profile ($n \propto r^{-2}$), the deceleration time at polar angle θ scales as $t_{\rm dec}(\theta) \propto \frac{\mathcal{E}(\theta)}{A_\star \Gamma_0(\theta)^4}$, while the SSC-dominated flux at a given epoch is strongly regulated by relativistic beaming, approximately $\propto a_{\rm dop}^3$.

Increasing E_k raises $\mathcal{E}(\theta)$ at all polar angles, thereby increasing the number of radiating nonthermal electrons and enhancing the synchrotron seed photon field. This directly boosts the SSC flux. For the on-axis case, the peak time is closely associated with the deceleration epoch and, therefore, scales approximately as $t_{\rm pk} \propto E_k$. Consequently, larger E_k produces brighter peaks that occur at later times, as shown in Fig. 2(a). For the off-axis scenario, the same intrinsic scaling is present but is partially dominated by Doppler deboosting. The peak occurs when $\Gamma(\theta_v) \sim 1/\theta_v$, introducing an additional geometric delay. As a result, off-axis peaks are systematically later and dimmer than their on-axis counterparts for the same E_k, although the monotonic increase of peak flux with E_k remains evident.

An increase in $A_\star$ enhances the external density at a given radius in the wind medium, increasing the number of swept-up electrons and strengthening both the comoving magnetic field and photon energy densities. This enhances the SSC flux. However, since $t_{\rm dec} \propto A_\star^{-1}$ in a wind environment, a larger $A_\star$ advances the deceleration epoch and shifts the TeV peak to earlier times. For on-axis observers, this results in an earlier and brighter SSC peak. In the off-axis case, although the intrinsic peak time shifts earlier with increasing $A_\star$, the geometric delay associated with $\Gamma \sim 1/\theta_v$ remains. Therefore, the off-axis peak continues to occur later and at lower flux compared to the corresponding on-axis case, even at higher $A_\star$.

In Fig. 2(c) we observe that, for the on-axis scenario, larger η_c increases the early-time beaming and advances the peak because $t_{\rm pk} \propto \Gamma_c^{-4}$. This is seen as the orange ($\eta_c = 540$) curve, which peaks slightly earlier and at a higher flux than the purple ($\eta_c = 340$) and gray ($\eta_c = 240$) curves, respectively. After the peak turnover, the curves converge as the flow becomes only mildly relativistic and beaming differences diminish, as discussed earlier. However, for the off-axis ($\theta_v > \theta_c$) scenario, with the same value of Γ_c, peak flux lowers compared to the on-axis case, and the observed peak shifts to a later time. Accordingly, the orange dashed-dot curve is brighter but peaks earlier than the lower Γ_c cases in the off-axis scenario.

Figure 3 shows TeV light curves for two distinct ratios of microphysical parameters ϵ_e/ϵ_B. With ϵ_B held fixed, increasing the ratio ϵ_e/ϵ_B means we vary ϵ_e to its higher and lower values, i.e., $\epsilon_e = \{10^{-2}, 10^{-1}\}$. All solid curves represent on-axis ($\theta_v < \theta_c$) and dash-dot depicts the off-axis ($\theta_v > \theta_c$) scenario. The raising ϵ_e/ϵ_B primarily boosts the SSC peak flux because of the increased Compton Y parameter [22,23], and $\gamma_m \propto \epsilon_e$ (see Sec. II B) elevates both the synchrotron seed photon field and the SSC flux. Consequently, the higher-ratio $\epsilon_e/\epsilon_B = 10^3$ orange light curves are brighter than the lower-ratio $\epsilon_e/\epsilon_B = 10^2$ purple light curves. The peak time, however, changes only marginally because variations in ϵ_e do not modify the deceleration dynamics. Thus, while microphysical parameters primarily regulate the amplitude of the SSC emission, the jet geometry and external density profile play the dominant role in determining the peak timing.

IV. DETECTABILITY OF TEV LIGHT CURVES IN WIND-DRIVEN MEDIUM WITH CTA SENSITIVITY

The CTAO Northern array differential sensitivity at 250 GeV is adopted from the sensitivity curves provided by the CTAO consortium.[2] These sensitivity curves represent the minimum detectable differential energy flux $E^2 dN/dE$ as a function of exposure time, assuming standard background conditions and a predefined detection significance. To explore TeV detectability in a stellar wind–driven medium, we simulate 4×10^4 afterglow light curves spanning a broad prior range of seven afterglow parameters. For each simulated event, the SSC emission predicted by the Gaussian structured jet model described in Sec. II is used to compute the differential energy flux at 250 GeV. The flux is averaged over successive observational intervals covering integration times relevant for GRB follow-up, from tens of seconds to several hours. A burst is considered detectable if, within at least one observational interval, the averaged flux exceeds the exposure-dependent CTA sensitivity threshold, as

$$\left\langle E^2 \frac{dN}{dE}(250\ \mathrm{GeV}) \right\rangle_{t_i,\Delta t_i} \geq F_{\rm sens}(250\ \mathrm{GeV}, \Delta t_i), \qquad (14)$$

where $\langle E^2 dN/dE \rangle_{t_i,\Delta t_i}$ denotes the time-averaged differential energy flux over the ith observational interval

[2] https://www.ctao.org/for-scientists/performance/

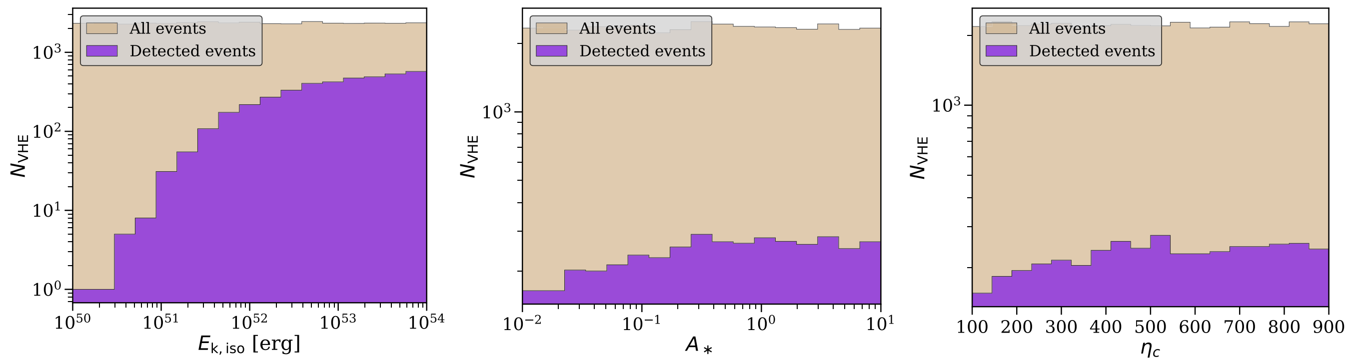

FIG. 4. Histograms showing the distribution of all CTA-detected events compared to all simulated samples for parameters E_k, $A_\star$, and η_c. These plots depict that higher values of E_k and $A_\star$ are more probable for CTA detections, whereas moderately high values of η_c favor CTA detectability.

beginning at observer time t_i and lasting for an exposure duration Δt_i. The sensitivity function $F_{\rm sens}(250\ {\rm GeV}, \Delta t_i)$ corresponds to the minimum detectable differential energy flux at 250 GeV for an exposure time Δt_i, as provided by the CTAO performance curves.

This framework provides an exposure-dependent sensitivity for CTA detectability that preserves the temporal scaling of instrumental sensitivity. The luminosity distance is fixed at $z = 0.5$ ($d_L \approx 2863.1$ Mpc) in order to isolate intrinsic parameter dependencies. All simulated SSC light curves include attenuation due to the extragalactic background light.

Our afterglow parameter space comprises the jet kinetic energy E_k, the wind density parameter $A_\star$, the microphysical parameters ϵ_e and ϵ_B, the jet structure parameters θ_c and θ_v, and the initial velocity η_c. For each simulated event, the afterglow parameters are sampled independently from prior distributions spanning ranges consistent with previous studies. We assume log-uniform priors for E_k, $A_\star$, ϵ_e, and ϵ_B over the ranges $E_k \in [10^{50}, 10^{54}]$ erg, $A_\star \in [10^{-3}, 1]$, $\epsilon_e \in [10^{-3}, 0.2]$, and $\epsilon_B \in [5 \times 10^{-7}, 10^{-2}]$. The angular parameters are taken to be uniformly distributed, with $\theta_c \in [1°, 13°]$ and $\theta_v \in [0°, 20°]$. Here, the Gaussian jet profile is truncated at an outer angle $\theta_j = 15°$, beyond which the energy per unit solid angle becomes negligibly small. This truncation ensures convergence of the angular integration while preserving the total jet energy. The initial Lorentz factor η_c is drawn from a uniform prior in the range [100, 900].

Based on these priors, we find that 4101(∼10.25%) out of 4×10^4 simulated events satisfy the CTA detectability criterion, meaning that the time-averaged differential energy flux at 250 GeV exceeds the exposure-dependent sensitivity threshold in at least one observational time bin. This underlines that VHE detections arise only from favorable regions of parameter space and exhibit strong dependence on both the external environment and microphysics. In particular, larger E_k and denser winds (larger $A_\star$) increase the typical SSC flux, while the detectability dependence on η_c reflects the competing roles of early-time brightness and spectral evolution (Fig. 4). Since EBL attenuation is included, the fraction of detectable events decreases with increasing luminosity distance, consistent with previous studies [22,23].

The microphysical parameters ϵ_e and ϵ_B play a decisive role in detection (Fig. 5). Larger ϵ_e increases the energy imparted to the nonthermal electrons, therefore, enhances the synchrotron luminosity and hence the SSC seed photon field within the same shocked region. Conversely, smaller ϵ_B reduces the magnetic field strength and tends to increase the Compton dominance (larger Y), favoring efficient SSC upscattering into the TeV band, subject to KN effects and EBL absorption. The jet geometry also strongly impacts detectability: as shown in Fig. 6, all the detected events are concentrated at small θ_v/θ_c (near-core viewing $\theta_v/\theta_c \lesssim 2$), and the detection fraction declines rapidly as θ_v/θ_c increases (beyond $\theta_v/\theta_c > 3$) for the adopted priors and fixed luminosity distance. Together, these trends demonstrate that CTA detectability requires a combination of favorable energetics, circumburst density, microphysical parameters, and observing geometry.

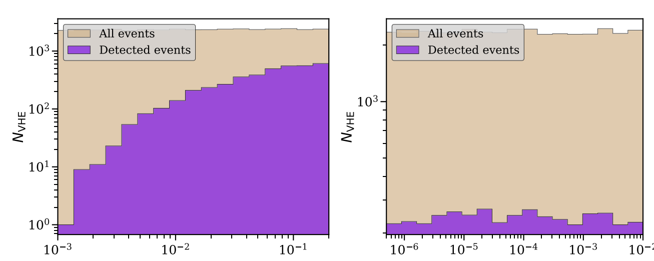

FIG. 5. Histograms illustrate that all CTA-detected events are more probable at higher values of ϵ_e (left), whereas the nearly uniform distribution in ϵ_B (right) indicates that this parameter has a weaker influence on CTA detectability.

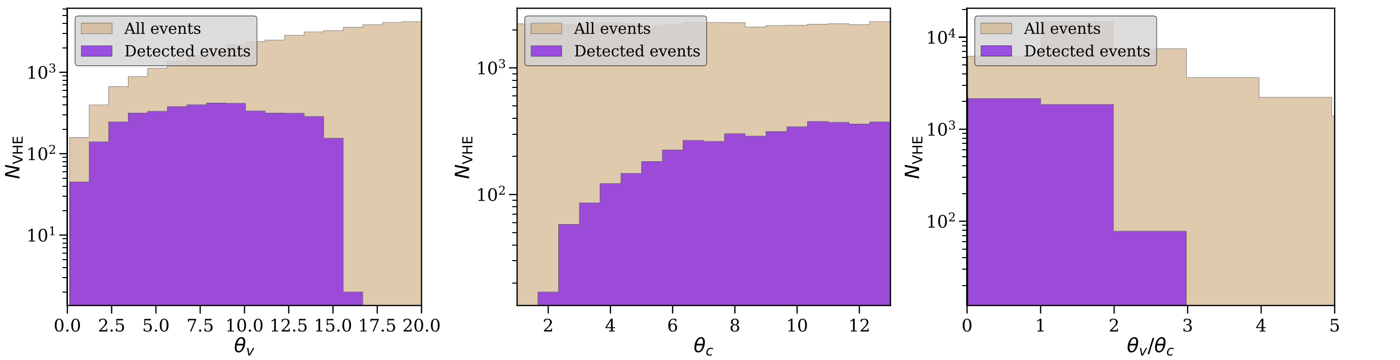

FIG. 6. Distribution of CTA-detected events compared to all simulated samples for parameters θ_v, θ_c, and θ_v/θ_c.

V. FITTING VHE DATA OF GRB 221009A IN WIND-DRIVEN MEDIUM

In Sec. II we developed the numerical framework describing TeV emission from an off-axis Gaussian structured jet propagating into a stellar wind medium. We now apply this framework to model the broadband afterglow of GRB 221009A. The goal is to reproduce the observed temporal evolution across multiple wavelength bands, ranging from radio and optical to x-ray, GeV, and TeV energies, and thereby constrain the physical parameters governing the jet dynamics and radiation processes.

A. Fitting method

As outlined in Sec. II, the peak flux and peak epoch of a GRB afterglow depend jointly on the jet dynamics, external density profile, and the viewing geometry. We model GRB 221009A with a Gaussian structured jet expanding into a stellar wind medium, characterized by the parameter set

$$\Theta_A = \{E_k, A_\star, \eta_c, \theta_j, \theta_c, \epsilon_e, \epsilon_B, p, \theta_v\},$$

with the luminosity distance fixed to $d_L = 723.6$ Mpc. For the light-curve fitting procedure we vary seven parameters while fixing the jet truncation angle and electron spectral index to $\theta_j = 15°$ and $p = 2.5$, respectively. The angle θ_j defines the outer boundary of the jet, beyond which the energy drops sharply and, therefore, has little impact on the observed afterglow evolution. The multiwavelength observational data used in this analysis include radio (1.3–90 GHz), optical (r and z bands), x-ray (0.3–10 keV), GeV (0.1–10 GeV), and TeV (0.3–5 TeV) measurements compiled from Ren *et al.* [34], Ren *et al.* [24], and LHAASO collaboration [50].

We infer the posterior distributions of the model parameters with a Bayesian MCMC analysis using the *emcee*[3] [51] Python package. The fitting procedure is performed jointly on the broadband light curves, including radio, optical, x-ray (Swift/XRT), GeV, and TeV observations, adopting broad, physically motivated uniform priors for all seven parameters. Assuming independent Gaussian measurement errors, the likelihood is constructed from the reported flux uncertainties in each band, and instrumental systematic errors are not included. Thus, we efficiently explore the multidimensional parameter space and achieve robust posterior credible intervals for the wind-structured jet model of GRB 221009A.

To obtain the temporal fit of GRB 221009A, we first constrain the afterglow parameters using the 0.1–10 GeV light curve, where the emission in our model is dominated by synchrotron self-Compton radiation. The parameter posteriors are sampled using the EMCEE MCMC sampler with 32 walkers and 2000 iterations. The resulting maximum likelihood parameters and their 1σ credible intervals are listed in Table I, and the joint posterior distributions are shown in the corner plot (Fig. 8).

The parameter region allowed by the 1σ posterior intervals is then used to compute the predicted synchrotron and SSC emission across other wavelengths. In particular, the model predictions are compared with the x-ray, TeV, optical, and radio observations shown in Fig. 7. Within this parameter space, the same set of physical parameters

TABLE I. Best-fit afterglow parameters obtained from the MCMC fit to the 0.1–10 GeV light curve of GRB 221009A. The listed values correspond to the maximum likelihood parameters, with uncertainties representing the 1σ credible ranges of the posterior distributions.

Parameter	Range
$\log_{10} E_k$	$53.49^{+0.38}_{-0.64}$
$\log_{10} A_\star$	$-0.15^{+0.55}_{-0.65}$
η_c	$399.99^{+2.62}_{-2.79}$
$\log_{10} \epsilon_e$	$-0.83^{+0.25}_{-0.32}$
$\log_{10} \epsilon_B$	$-6.02^{+0.069}_{-0.28}$
θ_v (deg)	$2.52°^{+2.06}_{-1.10}$
θ_c (deg)	$4.12°^{+1.95}_{-0.84}$

[3] https://emcee.readthedocs.io/en/stable/

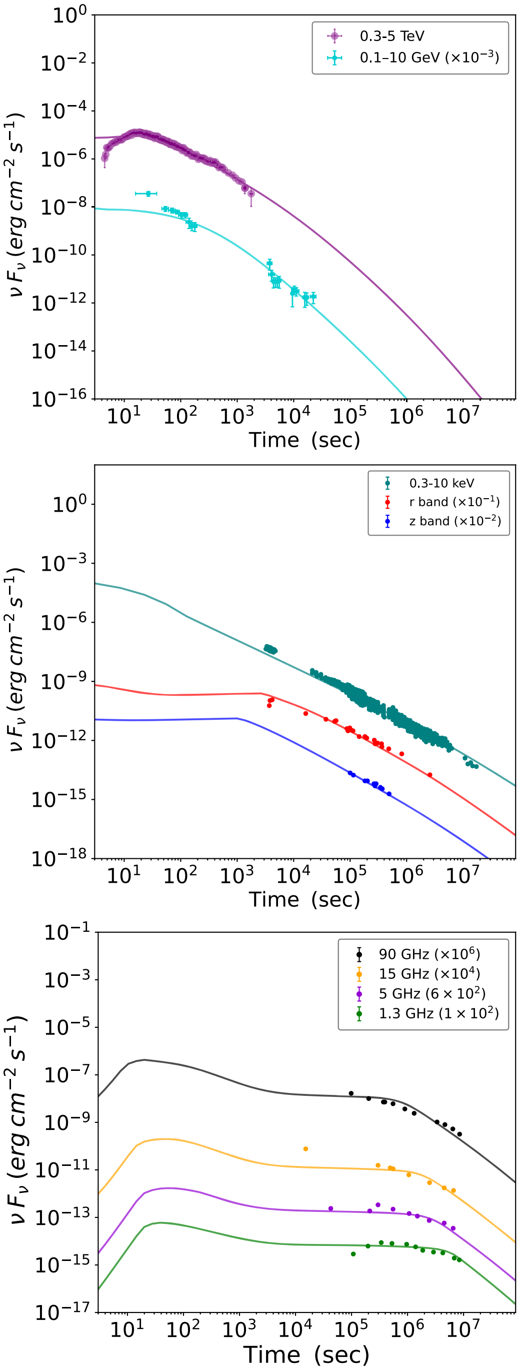

FIG. 7. Broadband multiband afterglow light curves of GRB 221009A spanning from TeV (0.3–5 TeV), GeV (0.1–10 GeV), x-ray (0.3–10 keV), optical (r and z bands), and radio (90 GHz, 15 GHz, 5 GHz, and 1.3 GHz) frequencies. The curves represent the best-fit light curves from the Gaussian structured jet model evolving in a wind-stratified medium. The high-energy GeV-TeV emission is dominated by SSC radiation, while the lower-energy bands from radio to x ray are primarily produced by synchrotron emission from the forward shock. The temporal evolution across multiple frequency bands constrains the jet structure, viewing geometry, and microphysical parameters governing particle acceleration and magnetic field.

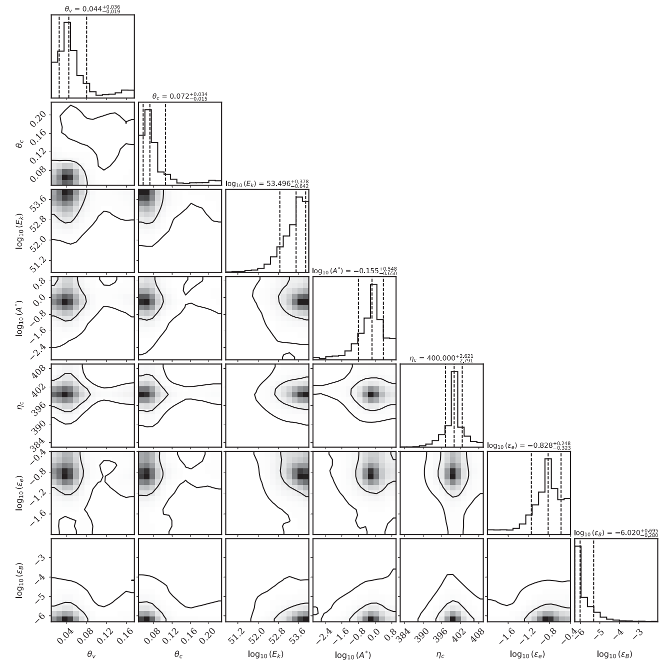

FIG. 8. Corner plot showing posterior distributions of afterglow model parameters for GRB 221009A. All the contours enclosing median values and $\pm 1\sigma$ uncertainties. Thin reference lines denote the truth values.

provides a consistent description of the broadband afterglow evolution from radio to TeV energies.

B. Temporal modeling of the GRB 221009A afterglow

In this work, we test the wind Gaussian structured jet framework using only the multiband light curves of GRB 221009A. Specifically, we perform a joint temporal fit to the x-ray (0.3−10 keV), GeV (0.1−10 GeV), and TeV (0.3 −5 TeV) data. The model computes synchrotron and SSC emission from a relativistic outflow with a Gaussian angular structure that decelerates in a stellar wind medium (see Sec. II). For the TeV band, we include KN corrections to the inverse-Compton cross section, and attenuation by the EBL. All light-curve fits are obtained with an MCMC sampler, and quoted parameter uncertainties correspond to the 1σ credible intervals from the posterior distributions (see Table I).

The resulting VHE light curves display the characteristic two-phase evolution of a decelerating blast wave: a gradual rise to peak followed by a steeper decay. Within the structured jet geometry, the temporal behavior is regulated by both dynamics (kinetic energy and ambient density) and geometry (viewing angle θ_v relative to the core width θ_c). A mildly off-axis configuration ($\theta_v/\theta_c \lesssim 2$) yields enhanced early-time VHE emission due to beaming from the energetic jet core, while larger θ_v/θ_c values suppress and delay the peak. The microphysical parameters also play a key role: fits consistently favor $\epsilon_e \gg \epsilon_B$, a regime that strengthens SSC relative to synchrotron at high energies and is required to reproduce the observed VHE SSC flux. In this model, the radio-optical x-ray emission is dominated by synchrotron radiation from the forward shock, while the GeV-TeV emission is primarily produced by synchrotron self-Compton scattering. Although our primary focus is the VHE SSC emission, the model simultaneously predicts the synchrotron counterpart from the same electron population. The radio, optical, and x-ray data, therefore, provide important constraints on the synchrotron component that supplies the seed photons for the SSC emission observed at GeV-TeV energies.

Figure 7 summarizes the broadband temporal fits across radio, optical, x-ray, GeV, and TeV bands. The model captures the rise, peak, and decay behavior and the relative timing offsets between the different energy bands that arise from the interaction of jet structure, blast-wave deceleration in a wind density profile, and KN and EBL suppression at the highest energies. The best-fit parameters inferred from the light curves are listed in Table I. Although our analysis shows that the Gaussian structured forward-shock model provides a reasonable description of the multiband afterglow, the radio emission of GRB 221009A has been suggested to require an additional low-frequency component beyond the standard forward-shock scenario [52]. Reverse-shock emission plays a crucial role in the radio afterglow of GRBs. However, for GRB 221009A, Laskar *et al.* [52] showed that the additional radio component cannot be straightforwardly identified with a standard reverse shock. They found that standard possibilities such as reverse-shock emission, a two-component jet, and thermal electron emission cannot satisfactorily reproduce the observed radio spectral and temporal evolution. In the present work, using the same best-fit parameter set (Table I) that describes the optical, x-ray, GeV, and TeV afterglow, our Gaussian structured forward-shock model also provides a reasonable description of the radio light curves at 90, 15, 5, and 1.3 GHz. We, therefore, do not introduce an explicit reverse-shock component in the present analysis, while noting that an additional low-frequency contribution may still be present in the radio emission. The inferred parameter set, characterized by a high kinetic energy E_k, moderate wind density parameter $A_\star$, and efficient electron acceleration ($\epsilon_e \gg \epsilon_B$), lies within the region of parameter space that favors TeV detectability with CTA, as explored in Sec. IV. For such configurations, the predicted SSC emission in the 0.3–5 TeV band reaches flux levels comparable to or exceeding the differential sensitivity of the CTA. This expectation is consistent with observational analyses of GRB 221009A by Abe *et al.* [53], which show that the intrinsic TeV afterglow emission in the 0.3–5 TeV energy band lies above the CTA(LST-1) sensitivity for early-time observations. The extreme energetics and favorable microphysical parameters inferred for this burst, therefore, place GRB 221009A among the most promising events for detection by next-generation Cherenkov telescopes.

VI. SUMMARY AND CONCLUSIONS

In this work, we developed an afterglow framework for modeling VHE emission from GRBs in which a Gaussian structured jet propagates into a stellar wind medium ($\rho \propto r^{-2}$). Within this framework we investigated how jet geometry, circumburst density, and microphysical parameters influence the production and detectability of SSC emission at high energies. We further applied the model to the broadband (radio, optical, x ray, GeV, and TeV) afterglow of GRB 221009A in order to constrain the physical conditions responsible for its exceptionally bright high-energy emission.

Through our numerical modeling, in Sec. II, we explored the temporal evolution of VHE SSC emission and found that the peak time and peak flux of the VHE light curves are strongly regulated by the viewing geometry through the ratio θ_v/θ_c. On-axis jet geometry produces early, bright TeV emission, whereas increasingly off-axis viewing angles lead to delayed, suppressed light curves due to relativistic beaming. The Gaussian angular structure provides a smooth transition between these regimes and allows improved constraints on the postpeak decay slopes across different viewing angles.

Our results further indicate that the VHE afterglow emission in this scenario favors a regime with $\epsilon_e \gg \epsilon_B$, consistent with SSC-dominated radiation at TeV energies. In addition to geometry, the jet energetics and the wind density parameter $A_\star$ also play a significant role in shaping the SSC light curves. In particular, modest variations in the viewing ratio θ_v/θ_c, jet kinetic energy E_k, or wind density parameter $A_\star$ can modify the predicted TeV flux by orders of magnitude. These dependencies highlight the strong sensitivity of VHE emission to both the jet structure and the properties of the circumburst wind environment, with direct implications for the detectability of GRB afterglows at TeV energies.

Motivated by these dependencies, in Sec. IV, we explored the detectability of such VHE afterglows with the CTA. Our results show that higher values of E_k, $A_\star$, and ϵ_e significantly enhance the probability of detection, while η_c and ϵ_B have comparatively moderate influence on the SSC emission in the CTA energy band. The jet geometry also plays a key role: increasing θ_v reduces the number of detectable events due to stronger relativistic deboosting, whereas larger jet core angles, θ_c, increase the overall detection probability. In particular, those with $\theta_v/\theta_c \lesssim 2$ provide the most favorable conditions for CTA detection in a wind-driven environment. The afterglow model parameters for CTA-detected cases follow trends similar to those reported by Mondal *et al.* [23].

We then applied this framework to the multiband observations of GRB 221009A, in Sec. V. The best-fit solution favors a mildly off-axis jet geometry in a wind medium with SSC-dominated high-energy emission. The temporal evolution of the afterglow is governed by the combined effects of jet energetics, wind density, microphysical parameters, and the viewing geometry, which regulates relativistic beaming and determines the observed peak flux and peak time. Within the 1σ credible region of the inferred parameters, the model well reproduces the observed radio, optical, x-ray, GeV, and TeV light curves of GRB 221009A. However, the possibility of reverse-shock emission in the low-frequency radio band remains relevant beyond the forward-shock emission suggested by Laskar *et al.* [52]. In the present work, we retain the Gaussian structured forward-shock model as the baseline framework, while a self-consistent treatment of possible reverse-shock emission, including the associated ejecta properties and microphysical parameters, will be addressed in our future work.

Several recent studies have also explored structured jet interpretations of GRB 221009A. Gill and Granot [37] modeled the multiwaveband x ray to radio afterglow using a power-law structured jet, finding a narrow jet core ($\sim 1.2°$) viewed close to the jet axis ($\sim 1.14°$). In contrast, our Gaussian structured jet model constrained by the GeV-TeV emission favors a moderately wider core ($\theta_c \sim 4.12°$) and a slightly larger viewing angle ($\theta_v \sim 2.52°$). O'Connor *et al.* [35] interpreted the late-time x-ray and optical/infrared evolution of the burst within a structured jet framework characterized by a shallow angular energy profile. Similarly, Ren *et al.* [34] analyzed the broadband afterglow using multiwavelength observations and demonstrated that the temporal evolution can be explained by a relativistic jet with angular structure viewed close to the jet axis. More recently, Ren *et al.* [24] modeled the broadband afterglow of GRB 221009A using a structured jet consisting of a top-hat inner core surrounded by a power-law outer wing structure. These studies collectively highlight the important role of jet structure and viewing geometry in interpreting the broadband afterglow behavior of GRB 221009A.

In this context, our results demonstrate that a Gaussian structured jet propagating in a wind-stratified medium provides a physically motivated framework for explaining both the broadband afterglow evolution and the production of VHE emission. This choice of circumburst environment is further supported by recent multiwavelength analyses of GRB 221009A, which report an increasing cooling break frequency at late times that is naturally expected in a windlike density profile [54], where $\nu_c \propto t^{1/2}$, rather than in a uniform ISM. Beyond reproducing the observed afterglow, our work provides a systematic investigation of how jet structure and the properties of the circumburst wind medium influence the generation and detectability of SSC emission at TeV energies. In particular, we find that the combination of a Gaussian angular jet profile and a wind-driven external medium naturally favors efficient SSC emission for moderately off-axis viewing geometries. Our analysis shows that the ratio θ_v/θ_c, together with the jet energetics and microphysical parameters, governs both the temporal evolution and the detectability of VHE afterglows. By exploring this parameter space, we identify regions where CTA is most sensitive to GRB afterglows and provide a physically motivated framework that connects the jet structure, the circumburst environment, and VHE radiation processes. In contrast to previous studies, our framework provides a predictive link between jet physics and the detectability of VHE emission. In particular, the inferred parameters for GRB 221009A fall within the region of parameter space that favors strong SSC emission in the TeV band, indicating that GRBs with similar energetics and microphysical parameters should be detectable by the CTA. Our results, therefore, suggest that future CTA observations of nearby GRBs will provide a powerful probe of relativistic jet structure and particle acceleration in extreme astrophysical outflows, offering a direct way to test structured jet SSC models in the VHE regime.

ACKNOWLEDGMENTS

T. M. gratefully acknowledges Prof. Jagdish Joshi of ARIES for his valuable suggestions and insightful discussions. T. M. also expresses sincere gratitude to Prof. Sonjoy Majumder of the Department of Physics, IIT Kharagpur, for his invaluable support in this work. T. M. and S. C. acknowledge the Prime Minister's Research Fellowship (PMRF). R. L. acknowledges the support of the Anusandhan National Research Foundation (ANRF) Grant No. CRG/2022/00803. The authors also gratefully acknowledge the use of the Paramshakti Supercomputing Facility at IIT Kharagpur, established under the National Supercomputing Mission, Government of India, for providing the high-performance computational resources essential to this work.

DATA AVAILABILITY

The data are not publicly available. The data are available from the authors upon reasonable request.

[1] E. Costa *et al.*, Discovery of an x-ray afterglow associated with the γ-ray burst of 28 February 1997, Nature (London) **387**, 783 (1997).

[2] S. R. Kulkarni *et al.*, The afterglow, redshift, and extreme energetics of the gamma-ray burst 990123: Evidence for beaming?, Nature (London) **398**, 389 (1999).

[3] P. Mészáros and M. J. Rees, Optical and long-wavelength afterglow from gamma-ray bursts, Astrophys. J. **476**, 232 (1997).

[4] J. van Paradijs *et al.*, Transient optical emission from the error box of the γ-ray burst of 28 February 1997, Nature (London) **386**, 686 (1997).

[5] D. A. Frail, S. R. Kulkarni, L. Nicastro, M. Feroci, and G. B. Taylor, The radio afterglow from the γ-ray burst of 8 May 1997, Nature (London) **389**, 261 (1997).

[6] R. Sari, T. Piran, and R. Narayan, Spectra and light curves of gamma-ray burst afterglows, Astrophys. J. **497**, L17 (1998).

[7] N. M. Lloyd and V. Petrosian, Synchrotron radiation as the source of gamma-ray burst spectra, Astrophys. J. **543**, 722 (2000).

[8] J. M. Burgess, D. Bégué, J. Greiner, D. Giannios, A. Bacelj, and F. Berlato, Gamma-ray bursts as cool synchrotron sources, Nat. Astron. **4**, 174 (2020).

[9] MAGIC Collaboration, Observation of inverse compton emission from a long γ-ray burst, Nature (London) **575**, 459 (2019).

[10] HESS Collaboration, A very-high-energy component deep in the γ-ray burst afterglow, Nature (London) **575**, 464 (2019).

[11] HESS Collaboration, Revealing x-ray and gamma ray temporal and spectral similarities in the GRB 190829A afterglow, Science **372**, 1081 (2021).

[12] LHAASO Collaboration, Very high-energy gamma-ray emission beyond 10 TeV from GRB 221009A, Sci. Adv. **9**, eadj2778 (2023).

[13] MAGIC Collaboration, Magic detection of GRB 201216C at $z = 1.1$, Mon. Not. R. Astro. Soc. **527**, 5856 (2024).

[14] J. Chiang and C. D. Dermer, Synchrotron and synchrotron self-compton emission and the blast-wave model of gamma-ray bursts, Astrophys. J. **512**, 699 (1999).

[15] C. D. Dermer, J. Chiang, and K. E. Mitman, Beaming, baryon loading, and the synchrotron self-comptoncomponent in gamma-ray bursts, Astrophys. J. **537**, 785 (2000).

[16] R. Sari and A. A. Esin, On the synchrotron self-compton emission from relativistic shocks and its implications for gamma-ray burst afterglows, Astrophys. J. **548**, 787 (2001).

[17] K. Murase, K. Toma, R. Yamazaki, and P. Mészáros, On the implications of late internal dissipation for shallow-decay afterglow emission and associated high-energy gamma-ray signals, Astrophys. J. **732**, 77 (2011).

[18] N. Fraija, R. B. Duran, S. Dichiara, and P. Beniamini, Synchrotron self-compton as a likely mechanism of photons beyond the synchrotron limit in GRB 190114C, Astrophys. J. **883**, 162 (2019).

[19] X.-Y. Wang, R.-Y. Liu, H.-M. Zhang, S.-Q. Xi, and B. Zhang, Synchrotron self-compton emission from external shocks as the origin of the sub-TeV emission in GRB 180720B and GRB 190114C, Astrophys. J. **884**, 117 (2019).

[20] E. Derishev and T. Piran, The physical conditions of the afterglow implied by magic's sub-TeV observations of GRB 190114C, Astrophys. J. Lett. **880**, L27 (2019).

[21] J. C. Joshi and S. Razzaque, Modelling synchrotron and synchrotron self-Compton emission of gamma-ray burst afterglows from radio to very-high energies, Mon. Not. R. Astro. Soc. **505**, 1718 (2021).

[22] T. Mondal, S. Pramanick, L. Resmi, and D. Bose, Probing gamma-ray burst afterglows with the cherenkov telescope array, Mon. Not. R. Astro. Soc. **522**, 5690 (2023).

[23] T. Mondal, S. Chakraborty, L. Resmi, and D. Bose, Follow-up of neutron star mergers with CTA and prospects for joint detection with gravitational-wave detectors, Astrophys. J. **983**, 35 (2025).

[24] J. Ren, Y. Wang, and Z.-G. Dai, Jet structure and burst environment of GRB 221009A, Astrophys. J. **962**, 115 (2024).

[25] A. de Ugarte Postigo, L. Izzo, G. Pugliese, D. Xu, B. Schneider, J. P. U. Fynbo, N. R. Tanvir, D. B. Malesani, A. Saccardi, D. A. Kann, K. Wiersema, B. P. Gompertz, C. C. Thoene, and A. J. Levan (Stargate Collaboration), GRB 221009A: Redshift from X-shooter/VLT, GRB Coordinates Netw. **32648**, 1 (2022), https://ui.adsabs.harvard.edu/abs/2022GCN.32648....1D.

[26] P. Veres, E. Burns, E. Bissaldi, S. Lesage, O. Roberts, F. G. Team *et al.*, GRB 221009A: Fermi GBM detection of an extraordinarily bright GRB, GRB Coordinates Netw **32636**, 1 (2022), https://ui.adsabs.harvard.edu/abs/2022GCN.32636....1V.

[27] M. A. Williams, J. A. Kennea, S. Dichiara, K. Kobayashi, W. B. Iwakiri, A. P. Beardmore, P. A. Evans, S. Heinz, A. Lien, S. R. Oates *et al.*, GRB 221009A: discovery of an exceptionally rare nearby and energetic gamma-ray burst, Astrophys. J. Lett. **946**, L24 (2023).

[28] S. Lesage, P. Veres, M. Briggs, A. Goldstein, D. Kocevski, E. Burns, C. Wilson-Hodge, P. Bhat, D. Huppenkothen, C. Fryer *et al.*, Fermi-GBM discovery of GRB 221009a: An extraordinarily bright GRB from onset to afterglow, Astrophys. J. Lett. **952**, L42 (2023).

[29] D. Frederiks, D. Svinkin, A. Lysenko, S. Molkov, A. Tsvetkova, M. Ulanov, A. Ridnaia, A. Lutovinov, I. Lapshov, A. Tkachenko *et al.*, Properties of the extremely energetic GRB 221009a from konus-wind and SRG/ART-XC observations, Astrophys. J. Lett. **949**, L7 (2023).

[30] D. Svinkin, D. Frederiks, A. Ridnaia, A. Lysenko, T. Cline, Konus-Wind Team, A. von Kienlin, X. Zhang, A. Rau, V. Savchenko, E. Bozzo, C. Ferrigno, INTEGRAL SPI-ACS Team, A. Goldstein, M. S. Briggs, C. Wilson-Hodge, Fermi Gbm Team, S. Barthelmy, J. Cummings, H. Krimm, D. Palmer, A. Tohuvavohu, and Swift-Bat Team, IPN triangulation of extremely bright GRB 221009A, GRB Coordinates Netw. **32641**, 1 (2022), https://ui.adsabs.harvard.edu/abs/2022GCN.32641....1S.

[31] Y. Huang, S. Hu, S. Chen, M. Zha, C. Liu, Z. Yao, Z. Cao *et al.*, LHAASO observed GRB 221009A with more than 5000 VHE photons up to around 18 TeV, GRB Coordinates Netw. **32677**, 1 (2022), https://ui.adsabs.harvard.edu/abs/2022GCN.32677....1H.

[32] K. Mooley, E. Nakar, K. Hotokezaka, G. Hallinan, A. Corsi, D. Frail, A. Horesh, T. Murphy, E. Lenc, D. Kaplan *et al.*, A mildly relativistic wide-angle outflow in the neutron-star merger event GW170817, Nature (London) **554**, 207 (2018).
[33] R. Margutti, E. Berger, W.-f. Fong, C. Guidorzi, K. Alexander, B. Metzger, P. Blanchard, P. Cowperthwaite, R. Chornock, T. Eftekhari *et al.*, The electromagnetic counterpart of the binary neutron star merger LIGO/Virgo GW170817. V. Rising x-ray emission from an off-axis jet, Astrophys. J. Lett. **848**, L20 (2017).
[34] J. Ren, Y. Wang, L.-L. Zhang, and Z.-G. Dai, The possibility of modeling the very high energy afterglow of GRB 221009a in a wind environment, Astrophys. J. **947**, 53 (2023).
[35] B. O'Connor, E. Troja, G. Ryan, P. Beniamini, H. Van Eerten, J. Granot, S. Dichiara, R. Ricci, V. Lipunov, J. H. Gillanders *et al.*, A structured jet explains the extreme GRB 221009A, Sci. Adv. **9**, eadi1405 (2023).
[36] Y. Sato, K. Murase, Y. Ohira, and R. Yamazaki, Two-component jet model for multiwavelength afterglow emission of the extremely energetic burst GRB 221009A, Mon. Not. R. Astron. Soc. **522**, L56 (2023).
[37] R. Gill and J. Granot, GRB 221009A afterglow from a shallow angular structured jet, Mon. Not. R. Astro. Soc. **524**, L78 (2023).
[38] R. A. Chevalier and Z.-Y. Li, Wind interaction models for gamma-ray burst afterglows: The case for two types of progenitors, Astrophys. J. **536**, 195 (2000).
[39] A. Panaitescu and P. Kumar, Analytic light curves of gamma-ray burst afterglows: Homogeneous versus wind external media, Astrophys. J. **543**, 66 (2000).
[40] J. Granot and P. Kumar, Constraining the structure of gamma-ray burst jets through the afterglow light curves, Astrophys. J. **591**, 1086 (2003).
[41] T. Mondal, S. Razzaque, J. C. Joshi, S. Majumder, and D. Bose, Multi messenger study of GRB 221009A with VHE gamma-ray and neutrino afterglow from a Gaussian structured jet, J. High Energy Astrophys. **53**, 100636 (2026).
[42] G. P. Lamb and S. Kobayashi, Electromagnetic counterparts to structured jets from gravitational wave detected mergers, Mon. Not. R. Astron. Soc. **472**, 4953 (2017).
[43] L. Resmi, S. Schulze, C. Ishwara-Chandra, K. Misra, J. Buchner, M. De Pasquale, R. Sánchez-Ramírez, S. Klose, S. Kim, N. Tanvir *et al.*, Low-frequency view of GW170817/GRB 170817A with the giant metrewave radio telescope, Astrophys. J. **867**, 57 (2018).
[44] R. A. Chevalier and Z.-Y. Li, Gamma-ray burst environments and progenitors, Astrophys. J. **520**, L29 (1999).
[45] J. Granot, A. Panaitescu, P. Kumar, and S. E. Woosley, Off-axis afterglow emission from jetted gamma-ray bursts, Astrophys. J. **570**, L61 (2002).
[46] B. Zhang, *The Physics of Gamma-Ray Bursts* (Cambridge University Press, Cambridge, 2018).
[47] T. E. Jacovich, P. Beniamini, and A. J. Van Der Horst, Modelling synchrotron self-Compton and Klein-Nishina effects in gamma-ray burst afterglows, Mon. Not. R. Astro. Soc. **504**, 528 (2021).
[48] E. Nakar, S. Ando, and Re'em Sari, Klein–Nishina effects on optically thin synchrotron and synchrotron self-Compton spectrum, Astrophys. J. **703**, 675 (2009).
[49] A. Dominguez, J. R. Primack, D. Rosario, F. Prada, R. Gilmore, S. Faber, D. Koo, R. Somerville, M. Pérez-Torres, P. Pérez-González *et al.*, Extragalactic background light inferred from AEGIS galaxy-SED-type fractions, Mon. Not. R. Astron. Soc. **410**, 2556 (2011).
[50] Z. LHAASO Collaboration, CAO, F. Aharonian, Q. An, Axikegu, L. Bai, Y. Bai, Y. Bao, D. Bastieri, X. Bi *et al.*, A tera-electron volt afterglow from a narrow jet in an extremely bright gamma-ray burst, Science **380**, 1390 (2023).
[51] D. Foreman-Mackey, D. W. Hogg, D. Lang, and J. Goodman, emcee: The MCMC Hammer, Publ. Astron. Soc. Pac. **125**, 306 (2013).
[52] T. Laskar, K. D. Alexander, R. Margutti, T. Eftekhari, R. Chornock, E. Berger, Y. Cendes, A. Duerr, D. A. Perley, M. E. Ravasio *et al.*, The radio to GeV afterglow of GRB 221009A, Astrophys. J. Lett. **946**, L23 (2023).
[53] K. Abe, S. Abe, A. Abhishek, F. Acero, A. Aguasca-Cabot, I. Agudo, C. Alispach, D. Ambrosino, F. Ambrosino, L. Antonelli *et al.*, GRB 221009A: Observations with LST-1 Of CTAO and implications for structured jets in long gamma-ray bursts, Astrophys. J. Lett. **988**, L42 (2025).
[54] D. Tak, Z. L. Uhm, G. S. H. Paek, M. Im, M. Arimoto, H. Choi, S. Kim, N. Omodei, J. Racusin, Y. Urata, and B. Zhang, Multiwavelength afterglow analysis of GRB 221009A: Unveiling the evolution of a cooling break in a wind-like medium, Astrophys. J. **978**, 29 (2025).